EXPERIMENTAL INVESTIGATIONS OF EXCITING FORCES CAUSED BY FLOW IN LABYRINTH SEALS*

G. Thieleke and H. Stetter
Institut für Thermische Strömungsmaschinen
und Maschinenlaboratorium
University of Stuttgart
Pfaffenwaldring 6
D-7000 Stuttgart 80, Federal Republic of Germany

The interaction of the flow through the labyrinth seals with the shaft of the rotor can have an effect on the stability of turbomachines. Thus, the excited forces, so–called cross forces or non–conservative forces, arise, which act perpendicular to the rotor eccentricity. This effect is caused by an unsymmetrical pressure distribution within the labyrinth cavities.

Experimental investigations are carried out for different types of labyrinth geometries: two staggered labyrinths with teeth on the stator and grooved rotor as well as a full and a convergent stepped labyrinth. These labyrinths can be found on the tip shrouding of bladings in steam or gas turbines. The following parameters are varied in the test–facility: geometry of the labyrinth seals (number of cavities, inlet region), shaft rotation, pressure difference on the seal, entry–swirl and eccentricity of the rotor.

The results are presented for stiffness coefficients of the labyrinth seals, leakage flow and circumferential flow in each cavity which was measured with special probes. Generally, the inlet swirl has the greatest influence on the coefficients of the seals. The experimental results are compared with theoretical results and are in good agreement.

*Work under this study of labyrinth seals has been sponsored partially by the Forschungsvereinigung Verbrennungskraftmaschinen e.V. (Research Association for Internal Combustion Engines), Frankfurt/Main, Federal Republic of Germany.

1 Nomenclature

A	Area
B	Height of labyrinth seal strip
c	Stiffness–term
c	Circumferential velocity of flow
c_{uo}	Inlet swirl
d	Damping–term
D	Diameter
E_0^*	Flow characteristic
e	Dimensioned eccentricity
F	Force
F_B	Reference force
f	Cross-sectional area of control volume
F_0	Cross-sectional area for centered shaft-position
g_i	Value of parameter of $\overline{K_Q^*}$
H	Local radial clearance
h_d	Hydraulic diameter
j	Complex unity
$k = C_R/(B + C_R)$	Factor of area change
K_Q	Cross force spring-coefficient
K_R	Restoring force spring-coefficient
m	Inertia–term
m, N	Number of cavities
$m_{R;S}, n_{R;S}$	Coefficients for friction factor
$\dot{m}$	Leakage flow
$\dot{m}_i$	Leakage flow per circumferential length
$\dot{M}_0$	Leakage flow for centered shaft-position
p	Pressure
P_0	Pressure before seal
P1	Position of probe
Q	Cross force
R	Restoring force
R	Gas constant
Re	Reynolds number
r, R_R	Shaft radius
$\Delta r, C_R$	Nominal clearance
T	Temperature
t	Time
t, L	Pitch of seal strips
u_w	Rotor peripheral velocity
$u = c/R_R\omega$	Dimensionless circumferential velocity of flow
U	Length on which shear stress acts
z	Number of seal strips
β^*	Flow coefficient
$\epsilon = e/C_R$	Eccentricity ratio, perturbation parameter
μ	Flow coefficient
ν	Kinematic viscosity

ρ Density of fluid
π Pressure ratio (p_a/p_0)
φ Peripheral angle
τ Dimensionless time
σ Shear stress
ω Shaft angular velocity
Ω Shaft precessional velocity

subscripts

0 zeroth-order component
1 first-order component
c cosine
i i-th chamber value
Q cross
R rotor, restoring
r radial-direction
S stator
s sine
u circumferential direction
w shaft
y y-direction
z z-direction
$-$ mean-value
$*$ dimensionless value

Not presented notations are declared in text.

2 Introduction

In order to carry out a thorough stability analysis of turbomachine rotors, it is essential to know all the forces causing oscillations. These forces, acting on the rotating subassembly units of the rotor shaft, can effect the stability behaviour in such a way that the operation is seriously disturbed or even impossible. The major causes for rotor instability are mostly exciting forces resulting from fluid–mechanisms, which are found in journal bearings and in labyrinth seals. The interaction between the flowing medium and the rotor shaft cause a transmission of energy to the flexural oscillation system. That leads to rotor–instability, if damping is not sufficient.

In order to be able to judge the stability qualities in advance, the engineer has to carry out oscillation analyses. For that he needs information about the dynamic characteristics of the seals which are characterized by stiffness, damping and inertia terms. When these properties are known the fluid–mechanisms can be described in a linear equation of motion, i.e., equation (1).

$$\begin{pmatrix} F_y \\ F_z \end{pmatrix} = \begin{pmatrix} c_{yy} & c_{yz} \\ c_{zy} & c_{zz} \end{pmatrix} \begin{pmatrix} y \\ z \end{pmatrix} + \begin{pmatrix} d_{yy} & d_{yz} \\ d_{zy} & d_{zz} \end{pmatrix} \begin{pmatrix} \dot{y} \\ \dot{z} \end{pmatrix} + \begin{pmatrix} m_{yy} & m_{yz} \\ m_{zy} & m_{zz} \end{pmatrix} \begin{pmatrix} \ddot{y} \\ \ddot{z} \end{pmatrix} \tag{1}$$

These quantities must be known in order to design the dynamics of turbomachines properly.

Experimental results of labyrinth seal forces have been presented by Benckert and Wachter [1], [2]. They investigated several multistage types of different labyrinth seals and found out that for long seals the shaft rotation has a great influence.

Childs and Scharrer [3] surveyed experimentally the dynamic characteristics of long straight through

labyrinths. On this test facility, the stiffness behaviour as well as the damping characteristics could be determined, since the rotor carries out an oscillation motion in addition to its rotational motion.

Leong and Brown [4] surveyed long straight through labyrinths with different cavity geometries. The seal strips were attached to the stator. Their results show, that with increasing peripheral velocity of the rotor, the cross–coupled stiffness coefficients decrease and can become even negative.

Rajakumar and Sisto [5] and Serkov [6] investigated the flow forces for short straight through labyrinths. They found out, that the inlet swirl compared to the shaft rotation has a great influence on the cross forces.

In reviewing previous experimental investigations, there is a clear need for testing of short prevalent labyrinth seals, which can be found on the tip shrouding of bladings in steam or gas turbines.

3 Test–Facility

The investigations are carried out on a labyrinth test–facility at the 'Institut für Thermische Strömungsmaschinen und Maschinenlaboratorium' of Stuttgart University. The test–facility was originally set up in [1], [2] and has now been modified to fit the changed requirements. Using this setup the inlet flow is the same as in the shroud ring seals of a real turbine stage (e.g., overlapping of guide– and rotor–bladings, radial streamline variation).

The cutaway (figure 16) shows one of the shroud ring seals with grooved rotor and teeth on the stator to be examined. The flow force in the labyrinth seals is always determined by integration of the measured pressure in axial direction and along the perimeter. In the axial direction each cavity is looked at individually and then all cavities are summed up. The reduction of these results to components gives the cross and the restoring force Q and R. The influence of the following parameters have been surveyed:

- *Inlet state before the first seal tip* π, c_{u0}. It depends on the pressure ratio being at the seal and the inlet swirl of the flow. A nozzle ring in conjunction with a vacuum assembly can produce different swirl components c_{u0}. The measuring of the resulting circumferential component of the labyrinth flow is made with three–hole-cylinder probes specially developed for this purpose (see figure 1). Since the probes are also used in the area of the labyrinth strips and near the rotor surface, the wall effect on the calibration factors, defined in figure 1, must be tested and taken into consideration. The test medium is air which expands to the ambient conditions.

- *Eccentricity of the rotor* ϵ. The eccentricity is varied from negative over the centered position to positive values.

- *Peripheral velocity of rotor* u_w. The rotational rotor speed is increased from $u_w = 0m/s$ upto over $u_w = 100m/s$. The influence of the direction of rotor rotation is likewise being tested.

- *Geometry of the seal.* Measurements are made with 15 different labyrinth configurations. They can be subdivided into three different types of labyrinths; grooved, interlocking and stepped labyrinths (figures 18). Besides the number of cavities, the inflow contour of the labyrinth was also varied.

Figure 2 shows a summary of variations of the test parameters.

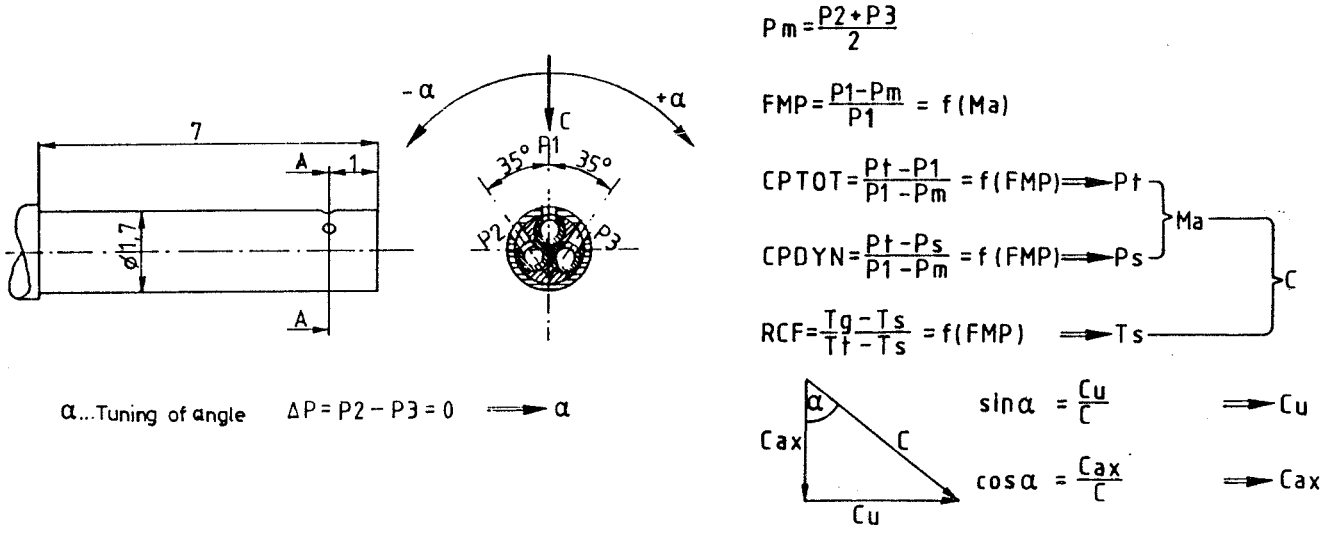

Figure 1: Three–hole-cylinder probe

Variation of Test Parameters					
inlet state	pressure ratio	p_a/p_0 [-]	0,5	0,3	0,25
	inlet swirl	c_{u0} [m/s]	0	80 3 steps	120
dimensionless rotor eccentricity $\epsilon = \frac{e}{\Delta r}$		ϵ [-]	+0,7	0 5 steps	−0,7
peripheral velocity of rotor		u_w [m/s]	+100	0 5 steps	−100

	typ	A1-3	G1	K1-7	M1-4
labyrinth geometry	number of cavites	7 5 4	3	4 3 (*) 2 (**) 1	8 7 5 3

(*) 2 variations of strips
(**) 3 variations of cavities

Figure 2: Variation of test parameters

4 Analysis of test data

The results are presented as follows:

- Variation of the flow forces in the individual cavity as dimensionless cross and restoring force in each cavity. The restoring force R_i^* acts against the rotor eccentricity ϵ (centering effect) and the cross force Q_i^* acts perpendicular to ϵ.
- Variation of the forces in the entire labyrinth as dimensionless cross force spring coefficient $\overline{K_Q^*}$ dependent on the test parameters and the flow characteristic E_0^*. The quantity E_0^* is the ratio of the inlet swirl energy and axial pressure drop.
- Leakage characteristic

The definitions for the calculation of the forces and the stiffness coefficients are summarized in figure 17.

5 Experimental Results

For the different labyrinth types of M– and A–configuration, the figures 19, 20 show the pressure distribution and the resulting rotor loads, i.e. cross and restoring force Q_i^* and R_i^*. The pressure distribution $p_i^*(\varphi)$ is related to the static pressure difference. For three eccentricities ($\epsilon = 0$ and $\epsilon \pm 0,66$), the pressure distributions depending on the individual labyrinth cavities and its circumferential angle φ are depicted. The flow conditions π, c_{u0}, u_w are noted in the figures.

For centered position ($\epsilon = 0$), the pressure distributions along the perimeter of the rotor are almost constant in the individual cavities. Thus, the resulting forces Q_i^* and R_i^* are nearly zero. But looking at the pressure drop in the axial direction shows, that the pressure drop depends on the geometry of the cavity (transitions of the staggered grooves). Figure 3 shows the resulting flow coefficient μ_i as a function of the cavity number i for the M1 to M4–configuration.

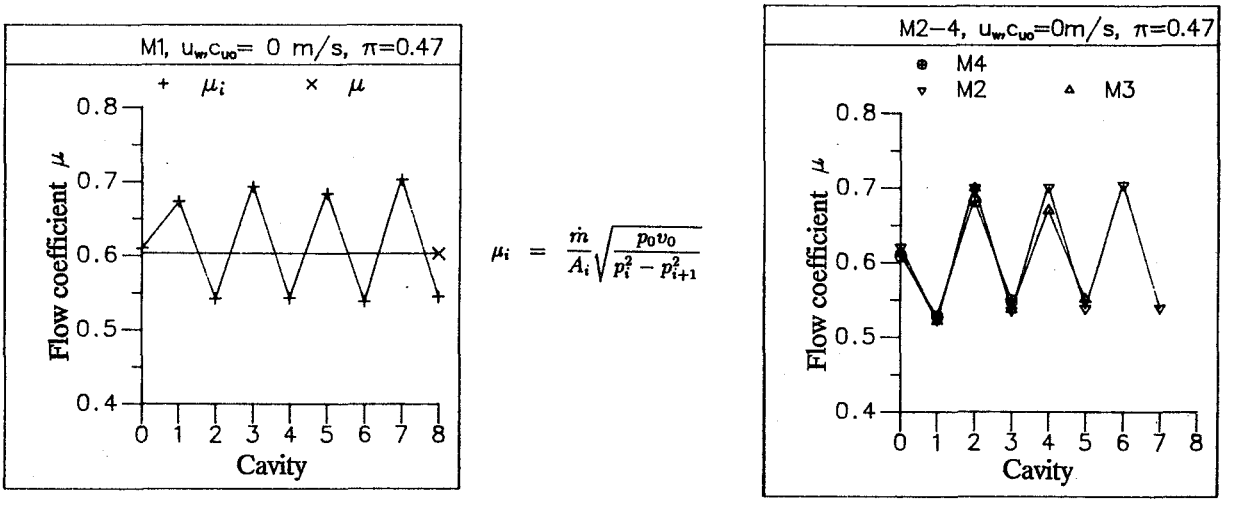

Figure 3: Flow coefficient μ_i of M1–M4–configurations

For positive and negative eccentricity ($\epsilon \pm 0,66$), the variations of pressure in the circumferential direction are almost identical. This correspondence for $\pm\epsilon$, which must come about for a perfect labyrinth geometry and an exactly adjusted rotor, is even more evident for Q_i^* and R_i^*.

The results show, that it is not the first cavity which provides the highest contribution of cross force. In the front part of the labyrinth, the cross force rises to its maximum and drops then continuously. For the M2–configuration the maximum is located in the 2. cavity (see figures 19, 21). This pattern is independent of inlet swirl, eccentricity and pressure rate. It was detected for all M–configurations. But the increase of the cross force in the front part depends on the inflow contour of the labyrinth. Relatively high gradients dQ_i^*/di were measured for the inflow contour with rotor groove and opposite long seal tip (M2 to M4–configuration). In figure 4 this is depicted for the M3 and M4–configuration.

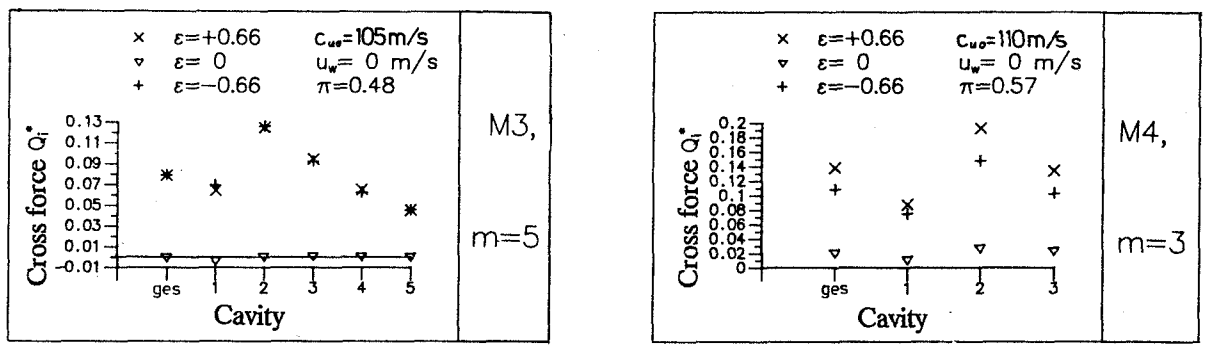

Figure 4: Cross force Q_i^* of M3– and M4–configuration

The increase of the cross force dQ_i^*/di is smaller for a inflow contour with rotor stage and opposite short seal tip (M1–configuration, see figure 5).

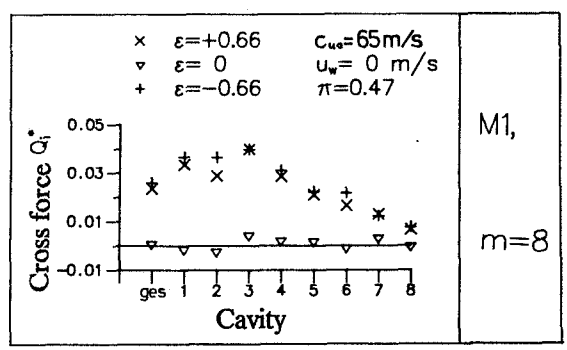

Figure 5: Cross force Q_i^* of M1–configuration

Apparently, the changed inflow geometry brings about a different inflow condition at the labyrinth. An extension of the space in front of the first seal tip results in a larger increase of the cross force in the front part of the labyrinth.

Like the experiments, analytical investigations show different cross force characteristics for each cavity when varying the boundary conditions. The boundary conditions are: the pressure distribution and the circumferential velocity distribution of the labyrinth flow along the perimeter in front of the first seal tip, and the flow coefficient μ_0. Furthermore, the boundary conditions at the exit of the labyrinth may also have an influence.

The influence of the inflow geometry on the cross force characteristics could be proved for the A–full–labyrinth as well (see fig. 6).

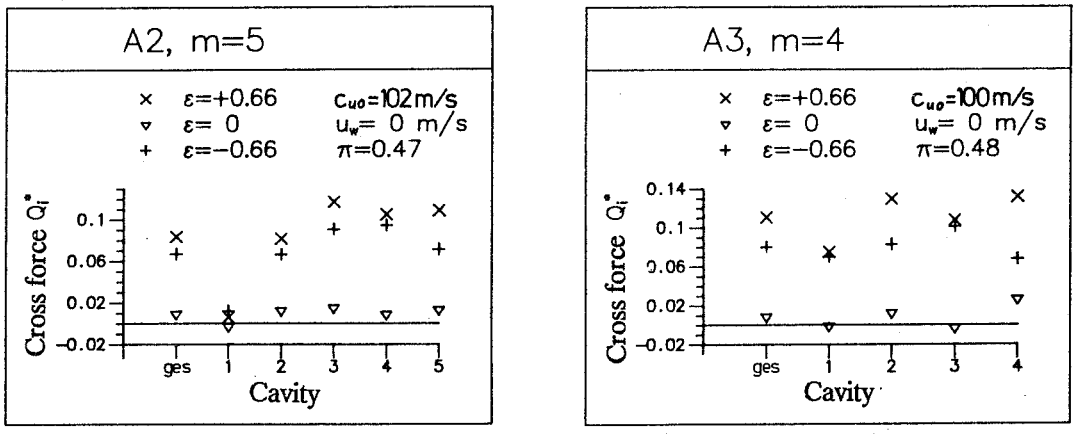

Figure 6: Cross force Q_i^* of A2– and A3–configuration

For the M2–configuration, fig. 21 shows the influence of the inlet swirl c_{u0} and the eccentricity ϵ on the cross force– and restoring force characteristics.

In contrast to Q_i^*, the restoring force is alternating along the cavities. Hence the resultant restoring force $\overline{R_i^*}$, recorded at the cavity number $i = ges$, is almost zero (see fig.7).

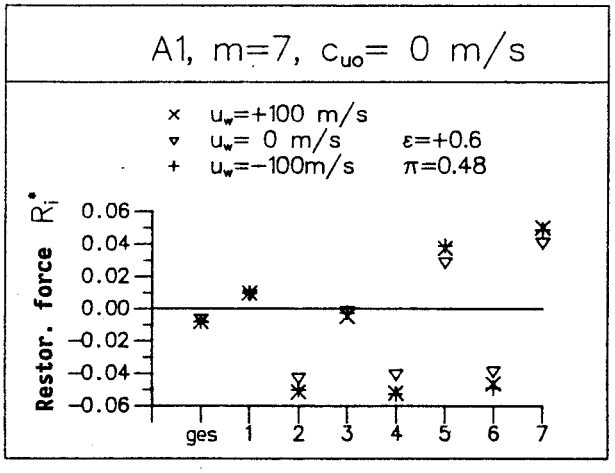

Figure 7: Restoring force R_i^* of A1–configuration

This characteristic is even more evident for the A–full–labyrinth. Pressure maxima and –minima respectively dependent on the cavity number occur in the area of the narrowest gap ($\varphi = 180°$). Similar to the Lomakin–effect [7], the losses due to friction and inflow respectively at each seal strip varying along the circumferential direction are responsible for that. That means, besides the dependence on the arrangement of the seal strips, the flow coefficient μ is also a function of the peripheral angle φ.

The alternating run of the restoring force R_i^* is independent from the peripheral velocity of the rotor. This is shown in figure 7 for the A1–configuration with 7 cavities and $c_{u0} = 0m/s$.

For the M1–(m=8) and M4–configuration (m=3) the figure 8 illustrates Q_i^* versus cavity number i for different u_w and superposed c_{u0}.

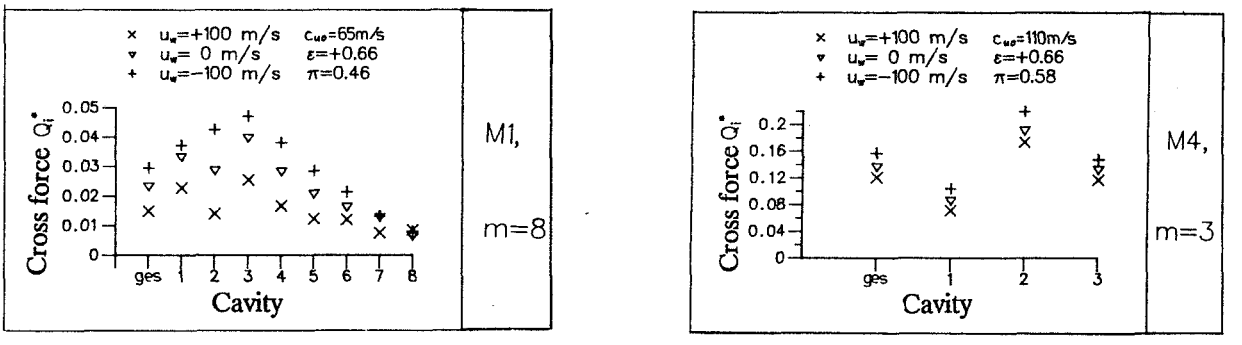

Figure 8: Cross force Q_i^* of M1– and M4–configuration

If the shaft rotates in the opposite direction of the inlet swirl, the value of u_w becomes negative. By definition the inlet swirl is positive in the direction of the peripheral angle φ. Changing the direction of u_w different situations in turbines and compressors can be simulated. Figure 8 shows that the cross force for $u_w = -95m/s$ is higher compared to $u_w = 0m/s$.

This effect can be explained by the ratio of decelerating to accelerating friction areas at rotor and stator. It has an effect on the distribution of the circumferential component of the labyrinth flow along the seal. The variation of c_u along the cavities shows that the amount of cross force doesn't depend on the amount of circumferential velocity of the labyrinth flow, but on the change of the circumferential flow between the cavities. For negative u_w the swirl changes are maximal (see fig. 9) and consequently the cross force as well.

With the help of flow–measuring probes it was ascertained that the circumferential component of the labyrinth flow is nearly not radial–changing within the cavities. Fig. 10 illustrates c_u versus the cavity number i for centered shaft position. Only in the vicinity of the stator surface the c_u–components are not constant. This is because of the effect of the boundary layer. Hence the circumferential velocity of the labyrinth flow in the cavities can be approximated by a mean circumferential velocity.

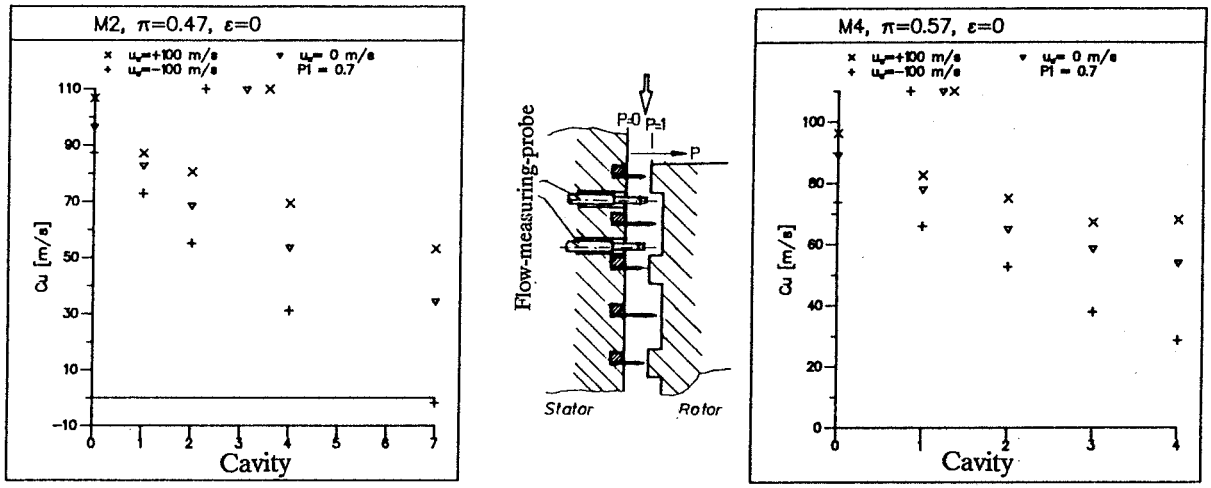

Figure 9: Circumferential velocity c_u with superposed rotor speed

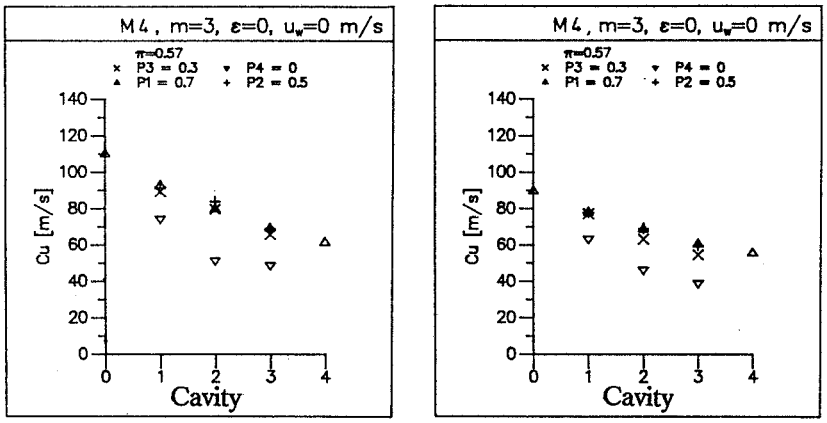

Figure 10: Circumferential velocity c_u of M4–configuration

Even for eccentric rotor position the c_u–components are almost constant in radial direction. Furthermore, fig. 25 shows for the M4–configuration the variation of c_u in the peripheral direction in each cavity. An approximation of c_u in terms

$$c_{u,i} = c_{um,i} + \epsilon \left(c_{u,c,i} \cos \varphi + c_{u,s,i} \sin \varphi \right) \tag{2}$$

confirms the assumptions of equations (9) and (11), see figure 25.

The relationship between the total cross force $\overline{Q^*}$ and the eccentricity ϵ is linear for all configurations as the plots in figure 11 show.

The characteristic field of the spring coefficient $\overline{K_Q^*}$ as a function of π, c_{u0} and u_w is shown in figure 22 and 23. These characteristic fields enable a separate investigation of the varied test parameters and its effects on the spring coefficient. It shows that the inlet swirl has the greatest influence on $\overline{K_Q^*}$.

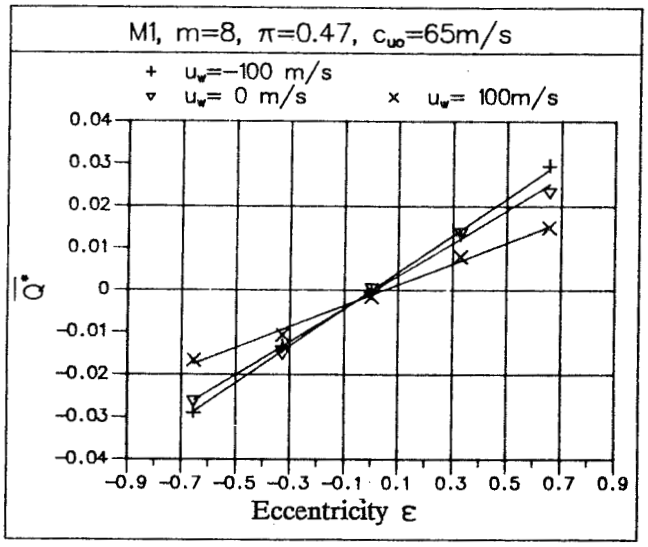

Figure 11: Cross force $\overline{Q^*}$ versus eccentricity ϵ of M1–configuration

Introducing the flow–characteristic E_0^*, the results can be transferred to seals in real machines. Fig. 12 shows for the M–configurations the obtained spring coefficients and the approximated curves. The approximating function is given by the nonlinear equation $\overline{K_Q^*} = g_1 + g_2 E_0^{*g_3}$. The coefficient g_1 corresponds to spring coefficient $\overline{K_Q^*}$ for axial inflow ($E_0^* = 0$).

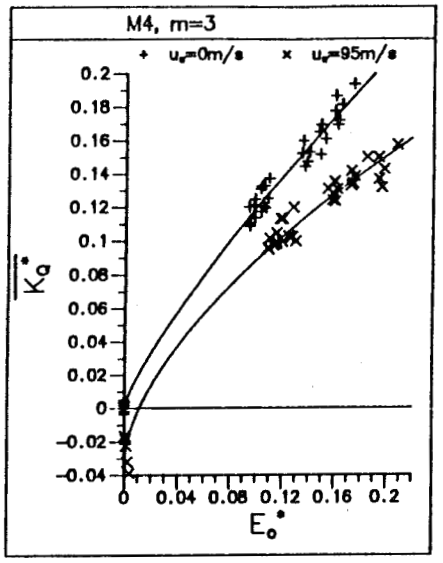

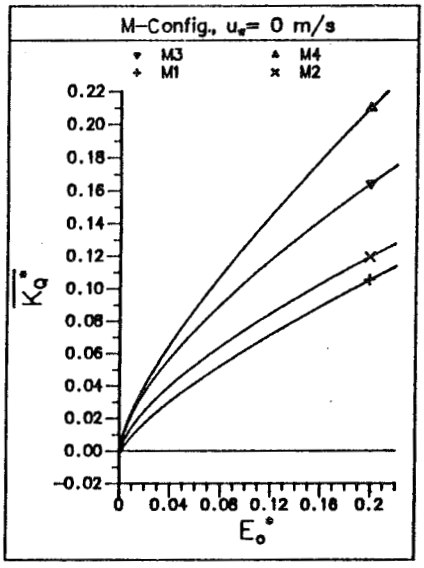

Figure 12: $\overline{K_Q^*}$ versus E_0^* of M–configuration

The comparison of the four M–configurations shows that the parameters $g_{1,2,3}$ depend on the number of cavities (see table 1).

In addition, table 1 shows the flow coefficient β^* for $E_0^* = 0$. The relationship between the leakage flow $\dot{m}$ and the flow coefficient β^* is:

$$\dot{m} = \beta^* \sqrt{\frac{\Delta r}{mt}} A_{res} \sqrt{\frac{p_0^2 - p_a^2}{p_0/\rho_0}}$$

Configurat.	u_w [m/s]	g_1	g_2	g_3	β^*
M1	0	-0,0031	0,3551	0,7336	1,9
M1	47	-0,0092	0,3809	0,7687	1,86
M1	94	-0,0115	0,4174	0,8252	1,79
M2	0	-0,0023	0,3533	0,6591	1,84
M2	47	-0,0081	0,3210	0,6489	1,82
M2	94	-0,018	0,298	0,60	1,76
M3	0	-0,0016	0,4726	0,6485	1,78
M3	47	-0,0139	0,4843	0,6710	1,76
M3	94	-0,0327	0,5091	0,6636	1,72
M4	0	0,0008	0,7586	0,8059	1,68
M4	47	-0,0109	0,5063	0,6472	1,67
M4	94	-0,0326	0,4826	0,6004	1,64
A1	0	0,0030	0,7316	0,8132	1,56
A1	47	0,0004	0,6954	0,7743	1,55
A1	94	0,0062	0,7616	0,8274	1,53
A2	0	0,0020	0,7747	0,8978	1,55
A2	47	0,0010	0,7132	0,8362	1,54
A2	94	-0,0007	0,6859	0,8046	1,52
A3	0	0,0044	1,0057	0,8812	1,45
A3	47	-0,0013	0,7879	0,7544	1,44
A3	94	-0,0058	0,7110	0,6955	1,42

Table 1: Values of the parameters $g_{1,2,3}$ $\overline{K_Q^*}$ and β^* of M– and A–labyrinth

Furthermore, the characteristic fields of the restoring force spring coefficient $\overline{K_R^*}$ as a function of the test parameters are depicted in the fig. 24.

6 Analysis

In order to compare the experimental with the theoretical results an analysis was developed. It bases on Iwatsubo's [8] and Child's [9] basic equations for compressible flow in a labyrinth seal. The continuity and momentum equation will be derived for a single cavity control volume as shown in figure 13.

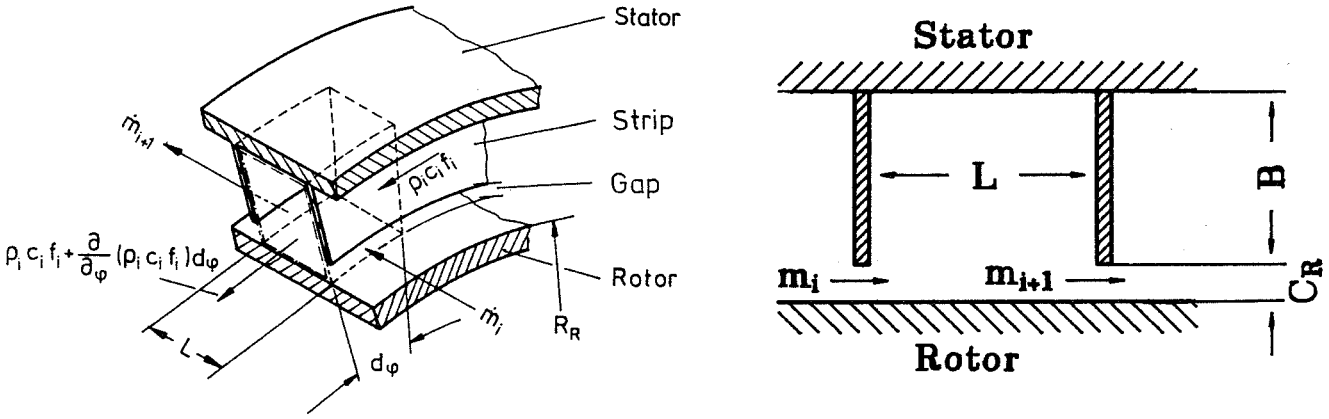

Figure 13: Cavity control volume

The governing equations are

- Continuity equation:

$$\frac{\partial}{\partial t}(\rho_i f_i) + \frac{1}{R_R}\frac{\partial}{\partial\varphi}(\rho_i f_i c_i) + \dot{m}_{i+1} - \dot{m}_i = 0 \tag{3}$$

- Momentum equation:

$$\begin{aligned}\frac{\partial}{\partial t}(\rho_i f_i c_i) &= -\frac{1}{R_R}\frac{\partial}{\partial\varphi}\left(\rho_i f_i c_i^2\right) - \frac{f_i}{R_R}\frac{\partial p_i}{\partial\varphi} + \dot{m}_i c_{i-1} - \dot{m}_{i+1} c_i \\ &\quad -\sigma_{t,Si} U_{Si} + \sigma_{t,Ri} U_{Ri}\end{aligned} \tag{4}$$

- Leakage equation:

$$\dot{m}_i = \mu_i H_i \sqrt{\frac{p_i^2 - p_{i+1}^2}{\mathrm{R}T}} \tag{5}$$

with leakage mass flow per circumferential length

- Friction equation:

$$\begin{aligned}\sigma_{t,Si} &= \frac{1}{2}\rho_i c_i^2 \lambda_{Si} = \frac{1}{2}\rho_i c_i^2 n_{Si}\left(\frac{|c_i| h_{di}}{\nu}\right)^{m_{Si}} \mathrm{sign}(c_i) \\ \sigma_{t,Ri} &= \frac{1}{2}\rho_i (R_R\omega - c_i)^2 \lambda_{Ri} \\ &= \frac{1}{2}\rho_i (R_R\omega - c_i)^2 n_{Ri}\left(\frac{|R_R\omega - c_i| h_{di}}{\nu}\right)^{m_{Ri}} \mathrm{sign}(R_R\omega - c_i)\end{aligned} \tag{6}$$

with h_d as hydraulic diameter.

- Ideal gas law:

$$\frac{p_i}{\rho_i} = \mathrm{R}T \tag{7}$$

- Normalization of the variables:

$$u_i = \frac{c_i}{R_R\omega} \qquad \tilde{p}_i = \frac{p_i}{P_0} \qquad \tilde{f}_i = \frac{f_i}{F_0} \qquad \dot{\tilde{m}}_i = \frac{\dot{m}_i}{\dot{M}_0} \qquad \tau = \omega t \tag{8}$$

The solution procedure is similar to the perturbation analysis used by Childs [10]:

- Linearized zeroth and first–order perturbation equations describe the pressure and velocity distributions for the centered (index '0') and eccentered (index '1') shaft position. The following perturbation variables are defined:

$$\begin{aligned} u_i &= u_{0,i} + \epsilon u_{1,i} \qquad \tilde{p}_i = p_{0,i} + \epsilon p_{1,i} \qquad \tilde{f}_i = f_{0,i} + \epsilon f_{1,i} \\ H_i &= C_R + \epsilon H_{1,i} \qquad \mu_i = \mu_{0,i} + \epsilon \mu_{1,i} \end{aligned} \tag{9}$$

  where $\epsilon = e/C_r$ is the eccentricity ratio.

- The zeroth–order solution for the circumferential velocity (zeroth–order momentum equation) is

$$\begin{aligned} 0 = {} & \frac{\mathrm{R}T\dot{M}_0}{\omega P_0}\left(u_{0,i-1} - u_{0,i}\right) \\ & -\frac{1}{2}R_R p_{0,i} u_{0,i}^2 n_{Si}\left(\frac{|u_{0,i}R_R\omega|h_{di}}{\nu}\right)^{m_{Si}} \mathrm{sign}(\omega u_{0,i}) U_{Si} \\ & +\frac{1}{2}R_R p_{0,i}\left(1-u_{0,i}\right)^2 n_{Ri}\left(\frac{|\left(1-u_{0,i}\right)R_R\omega|h_{di}}{\nu}\right)^{m_{Ri}} \mathrm{sign}\left(\omega\left(1-u_{0,i}\right)\right) U_{Ri} \end{aligned} \tag{10}$$

The partial differential equations (first–order solution) will be reduced to linear complex equations by introducing the following assumptions for the perturbation variables:

- Elimination of circumferential angle φ:

$$\begin{aligned} p_{1,i} &= p_{1,i,c}\cos\varphi + p_{1,i,s}\sin\varphi \qquad u_{1,i} = u_{1,i,c}\cos\varphi + u_{1,i,s}\sin\varphi \\ h_{1,i} &= \frac{H_{1,i}}{C_R} = -y_i\cos\varphi - z_i\sin\varphi \qquad \mu_{1,i} = \mu_{1,i,c}\cos\varphi + \mu_{1,i,s}\sin\varphi \end{aligned} \tag{11}$$

- Complex variables:

$$\begin{aligned} \underline{p}_{1,i} &= p_{1,i,c} + jp_{1,i,s} \qquad \underline{u}_{1,i} = u_{1,i,c} + ju_{1,i,s} \\ \underline{h}_{1,i} &= -y_i - jz_i \qquad \underline{\mu}_{1,i} = \mu_{1,i,c} + j\mu_{1,i,s} \end{aligned} \tag{12}$$

- Elimination of time t with harmonic seal motion (circular orbit with frequency Ω around the centered position, see fig. 14) :

$$\underline{h}_{1,i} = \hat{\underline{h}}_{1,i}e^{j\Omega t} \tag{13}$$

  and corresponding response for the other perturbations variables:

$$\begin{aligned} \underline{u}_{1,i} &= \hat{\underline{u}}_{1,i}e^{j\Omega t} = \hat{\underline{u}}_{1,i}e^{j\frac{\Omega}{\omega}\tau} \\ \underline{p}_{1,i} &= \hat{\underline{p}}_{1,i}e^{j\frac{\Omega}{\omega}\tau} \qquad \underline{\mu}_{1,i} = \hat{\underline{\mu}}_{1,i}e^{j\frac{\Omega}{\omega}\tau} \end{aligned} \tag{14}$$

  yields to the complex continuity and momentum equation:

- Complex continuity equation:

$$\begin{aligned}
&\left(j\frac{\Omega}{\omega} - ju_{0,i} + \frac{\mathrm{R}T\dot{M}_0}{\omega P_0 F_0}\left(\frac{p_{0,i}}{p_{0,i}^2 - p_{0,i+1}^2} + \frac{p_{0,i}}{p_{0,i-1}^2 - p_{0,i}^2}\right)\right)\hat{\underline{p}}_{1,i} \\
&-\frac{\mathrm{R}T\dot{M}_0}{\omega P_0 F_0}\frac{p_{0,i+1}}{p_{0,i}^2 - p_{0,i+1}^2}\hat{\underline{p}}_{1,i+1} - \frac{\mathrm{R}T\dot{M}_0}{\omega P_0 F_0}\frac{p_{0,i-1}}{p_{0,i-1}^2 - p_{0,i}^2}\hat{\underline{p}}_{1,i-1} - jp_{0,i}\hat{\underline{u}}_{1,i} \\
= &\left(jkp_{0,i}\left(u_{0,i} - \frac{\Omega}{\omega}\right) + \frac{\mathrm{R}T\dot{M}_0}{\omega P_0 F_0}\right)\hat{\underline{h}}_{1,i} \\
&-\frac{\mathrm{R}T\dot{M}_0}{\omega P_0 F_0}\hat{\underline{h}}_{1,i+1} + \frac{\mathrm{R}T\dot{M}_0}{\omega P_0 F_0}\left(\frac{\hat{\underline{\mu}}_{1,i}}{\mu_{0,i}} - \frac{\hat{\underline{\mu}}_{1,i+1}}{\mu_{0,i+1}}\right)
\end{aligned} \tag{15}$$

- Complex momentum equation:

$$\begin{aligned}
&-\frac{\mathrm{R}T\dot{M}_0}{\omega P_0 F_0}\frac{p_{0,i-1}\left(u_{0,i-1} - u_{0,i}\right)}{p_{0,i-1}^2 - p_{0,i}^2}\hat{\underline{p}}_{1,i-1} \\
&+\left(\frac{\mathrm{R}T\dot{M}_0}{\omega P_0 F_0}\frac{p_{0,i}\left(u_{0,i-1} - u_{0,i}\right)}{p_{0,i-1}^2 - p_{0,i}^2} - j\frac{\mathrm{R}T}{R_R^2\omega^2}\right. \\
&\left.-\frac{1}{2}\frac{R_R}{F_0}\left(U_{Ri}n_{Ri}\mathrm{Re}_{Ri}^{m_{Ri}}\left(u_{0,i} - 1\right)^2\,\mathrm{sign}(\omega(1 - u_{0,i})) - U_{Si}n_{Si}\mathrm{Re}_{Si}^{m_{Si}}u_{0,i}^2\mathrm{sign}(\omega u_{0,i})\right)\right)\hat{\underline{p}}_{1,i} \\
&-\frac{\mathrm{R}T\dot{M}_0}{\omega P_0 F_0}\hat{\underline{u}}_{1,i-1} \\
&+\left(jp_{0,i}\frac{\Omega}{\omega} - jp_{0,i}u_{0,i} + \frac{\mathrm{R}T\dot{M}_0}{\omega P_0 F_0} - \frac{R_R}{F_0}p_{0,i}\left(U_{Ri}n_{Ri}\mathrm{Re}_{Ri}^{m_{Ri}}\left(u_{0,i} - 1\right)\mathrm{sign}(\omega(1 - u_{0,i}))\right.\right. \\
&\left.\left.-U_{Si}n_{Si}\mathrm{Re}_{Si}^{m_{Si}}u_{0,i}\mathrm{sign}(\omega u_{0,i})\right)\right)\hat{\underline{u}}_{1,i} \\
= &\left(\frac{\mathrm{R}T\dot{M}_0}{\omega P_0 F_0}\left(u_{0,i-1} - u_{0,i}\right)\right)\hat{\underline{h}}_{1,i} + \frac{\mathrm{R}T\dot{M}_0}{\omega P_0 F_0}\left(u_{0,i-1} - u_{0,i}\right)\frac{\hat{\underline{\mu}}_{1,i}}{\mu_{0,i}}
\end{aligned} \tag{16}$$

- With equations (15), (16) a system equation for all cavities is formed and solved by linear equation algorithms. As a result the values of the complex amplitude $\hat{\underline{p}}_{1,i}$ and $\hat{\underline{u}}_{1,i}$ ($\hat{\underline{p}}_{1,i} = \hat{p}_{1,ic} + j\hat{p}_{1,is}$) are found.

- The flow force for the seal (see equation (1)) is found by integrating the first–order pressure perturbation along and around the shaft of the rotor. For the i-th cavity it is

$$\begin{aligned}
F_{y,i}(t) &= -P_0 R_R \epsilon\pi \int_0^L \left(\hat{p}_{1,ic}\cos\Omega t - \hat{p}_{1,is}\sin\Omega t\right) dx \\
F_{z,i}(t) &= -P_0 R_R \epsilon\pi L\left(\hat{p}_{1,i,c}\sin\Omega t + \hat{p}_{1,i,s}\cos\Omega t\right)
\end{aligned} \tag{17}$$

- Introducing a rotating coordinate–system (see figure 14) the rotating forces are

$$F_{r,i} = -P_0 R_R \epsilon\pi L\hat{p}_{1,i,c} \qquad F_\varphi = -P_0 R_R \epsilon\pi L\sum_{i=1}^{N}\hat{p}_{1,i,s} \tag{18}$$

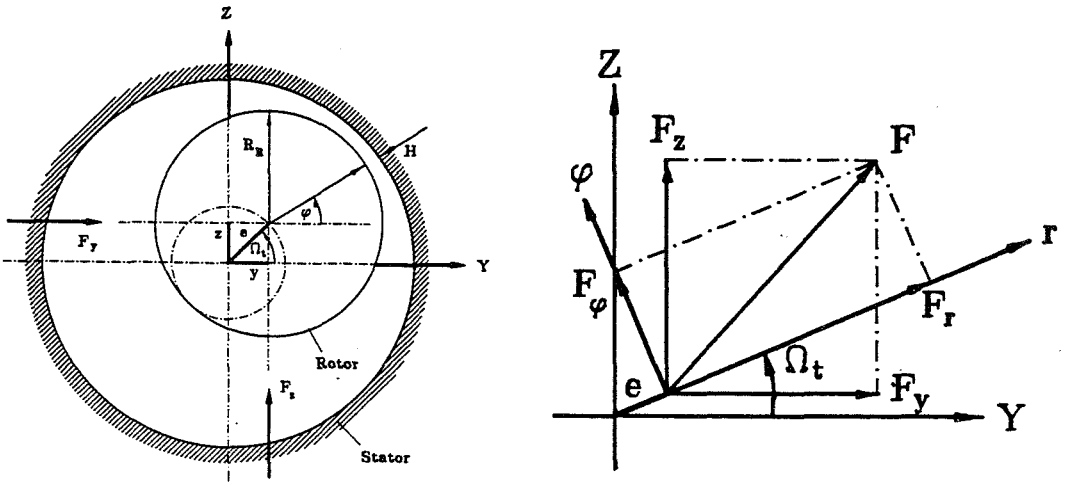

Figure 14: Harmonic seal motion and transformation of the coordinate system

- With the assumed orbit about the centered position the structure of the matrices of equation (1) becomes

$$c_{yy} = c_{zz},\ c_{yz} = -c_{yz}; \qquad d_{yy} = d_{zz},\ d_{yz} = -d_{yz}; \quad \ldots \tag{19}$$

- The searched coefficients can be found by a least square fitting for different frequencies of Ω:

$$\begin{aligned} F_r &= \epsilon C_r \left(c_{yy} + d_{yz}\Omega - m_{yy}\Omega^2\right) \\ F_\varphi &= -\epsilon C_r \left(c_{yz} - d_{yy}\Omega - m_{yz}\Omega^2\right) \end{aligned} \tag{20}$$

7 Comparison of the Results

Comparisons of theoretical and experimental results of the exciting cross–coupled stiffness coefficient c_{yz} respectively spring coefficients $\overline{K_Q^*}$ are made for the staggered labyrinth, configuration M4. The correlation is as follows:

$$\overline{K_Q^*} = -\frac{c_{yz} C_R}{\Delta p_{st} R_R m L} \tag{21}$$

The results are presented for $\overline{K_Q^*}$ as a function of the flow characteristic E_0^*. The friction parameters (see equation (6)) for the evaluations are set to

$n_{Ri} = 0,079 \qquad m_{Ri} = -0,25 \qquad n_{Si} = 0,15 \qquad m_{Si} = -0,25.$

The other input data like flow coefficient μ_i and boundary conditions are derived from experimental results, see figure 3.

The results are in good agreement with the spring coefficients $\overline{K_Q^*}$ (see figure 15).
Furthermore, an identification algorithm is currently under development. Its aim is to determine the friction factors $n_{R;Si}$ and $m_{R;Si}$ for each cavity based on the zeroth–order solution for the circumferential velocity (see quation (10)) of the staggered labyrinth . The first results (see figure 23) confirm the assumptions of this bulk–flow-theory, equations (9), (11).

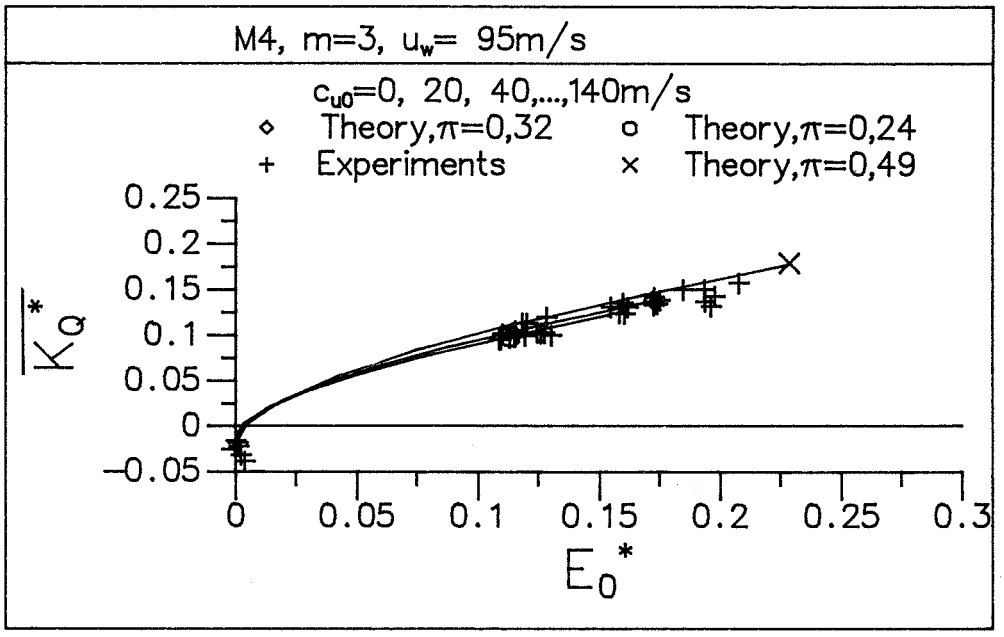

Figure 15: Comparison of theory and experiment

8 Conclusions

Experimental results have been presented for stiffness coefficients and leakage flow of different types of labyrinth geometries, such as grooved, interlocking and convergent stepped labyrinths. The influence of rotor speed, pressure ratio, inlet swirl and labyrinth geometry on the coefficients has been investigated.

The results of this study support the following conclusions:

- The cross force and restoring force are linear to eccentricity. Thus, the force–motion equation (1) is confirmed experimentally.
- The inlet swirl has the greatest influence on the cross–coupled stiffness coefficient $\overline{K_Q^*}$.
- The relationship between $\overline{K_Q^*}$ and the flow characteristic E_0^* depends on the test parameters.
- The cross force in each cavity depends on the change of circumferential velocity from cavity to cavity.
- The restoring force shows an alternating behaviour along the seal. Thus, the total restoring force is nearly zero.
- The results of the presented analysis are in good agreement with the experimental results. The experiments verify the assumptions of the analysis.

References

[1] Benckert,H.: Strömungsbedingte Federkennwerte in Labyrinthdichtungen. Diss. Univ. Stuttgart, 1980

[2] Benckert,H.,Wachter,J.: Flow Induced Spring Coefficients of Labyrinth Seals for Applications in Rotordynamic. NASA Conference Publication 2133, Rotordynamic Instability Problems in High–Performance Turbomachinery 1980

[3] Childs,D.W., Scharrer J.K.: Experimental Rotordynamic Coefficient Results for Teeth–on–Rotor and Teeth–on–Stator Labyrinth Gas Seals. Trans. ASME (Journal of Engineering for Gas Turbines and Power) Vol. 108 (1986) S.599-604

[4] Leong, Y.M.M.S. ,Brown,R.D.:Experimental Investigations of Lateral Forces Induced by Flow Through Model Labyrinth Glands. NASA Conference Publication 2338, Rotordynamic Instability Problems in High–Performance Turbomachinery 1984

[5] Rajakumar,C., Sisto,F.: Experimental Investigations of Rotor Whirl Excitation Forces Induced by Labyrinth Seal Flow. 11th ASME Biennial Conference on Mechanical Vibration and Noise 1987, S.263-272

[6] Serkov,S.A.: Die Bestimmung von aerodynamischen Kräften in Turbinendichtungen zur Erhöhung der Grenzstabilität. Wärme, Vol.92, 1986, No.4-5, S.79-83

[7] Lomakin,A.A.: Calculation of Critical Speed and Securing of the Dynamic Stability of the Rotor of Hydraulic High Pressure Machines with References to Forces Arising in Seal Gaps. Energomashinostrojenie 4, 1958, H. 4, S. 1-5

[8] Iwatsubo,T.,Matooka,N., Kawai,R.: Flow Induced Force of Labyrinth Seal. NASA Conference Publication 2250, Rotordynamic Instability Problems in High–Performance Turbomachinery 1982

[9] Childs,D.W.,Scharrer,J.K.: An Iwatsubo–Based Solution for Labyrinth Seals: Comparison to Experimental Results. Trans. ASME (Journal of Engineering for Gas Turbines and Power) Vol.108 (1986) S.325-331

[10] Childs,D.W., Chang–Ho Kim: Analysis and Testing for Rotordynamic Coefficients of Turbulent Annular Seals with Different, Directionally Homogeneous Surface–Roughness Treatment for Rotor and Stator Elements. NASA Conference Publication 2338, Rotordynamic Instability Problems in High–Performance Turbomachinery 1984

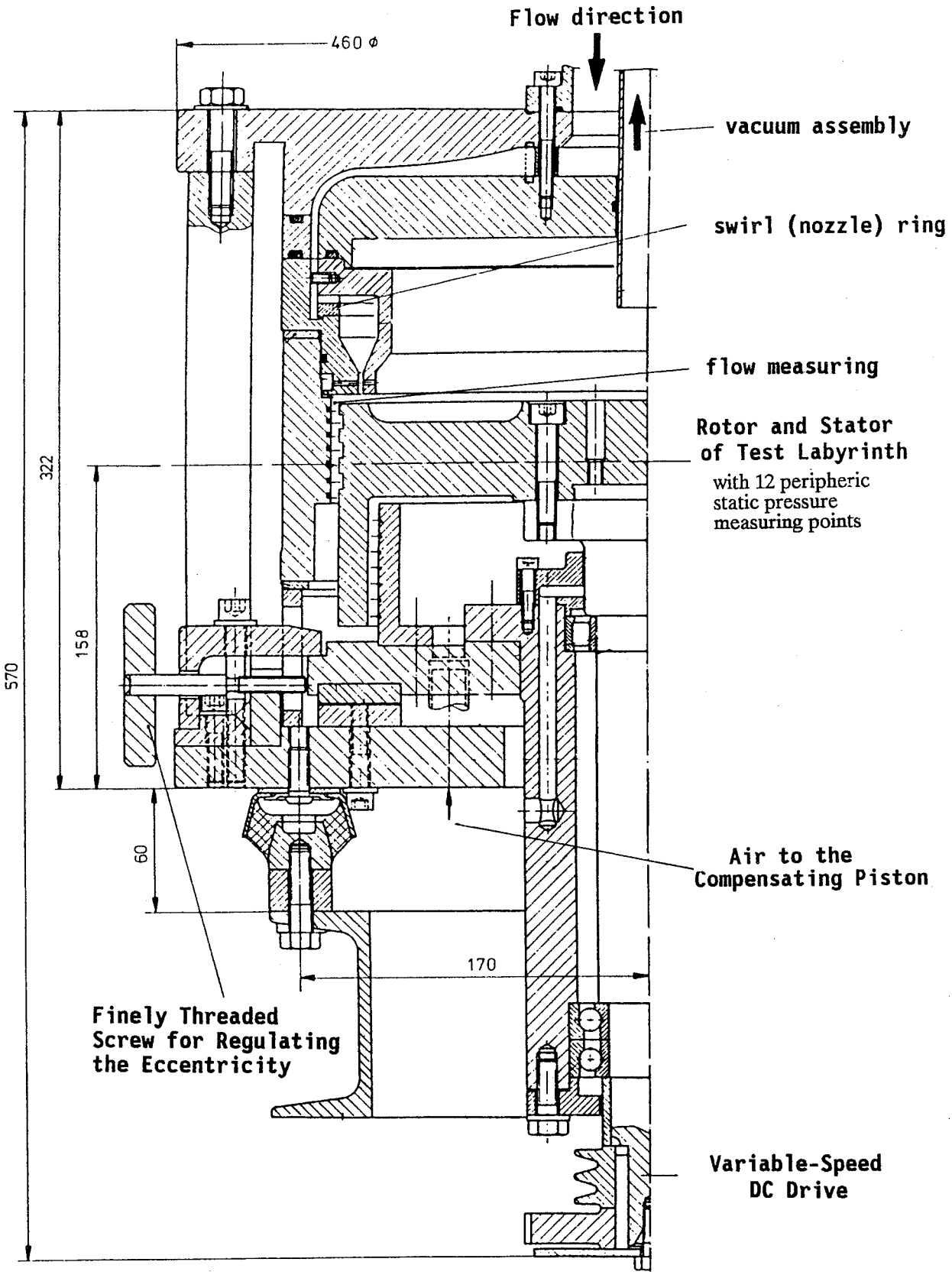

Figure 16: Testing facility of labyrinths

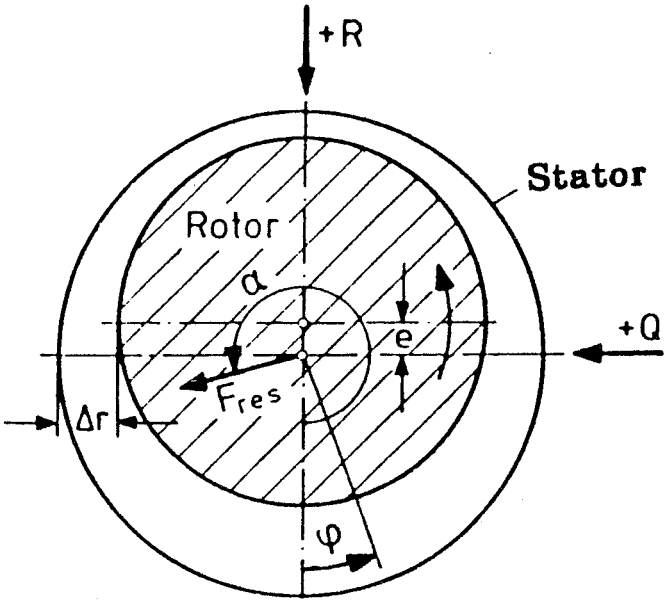

Inlet state	:	(p_0, T_0, c_{u0})		
Static pressure difference	:	Δp_{st}	=	$p_0 - p_a$
Relative pressure per cavity i	:	$p_i^*(\varphi)$	=	$(p_i(\varphi) - p_a)/\Delta p_{st}$
Flow characteristic	:	E_0^*	=	$\frac{1}{2}\rho_0 c_{u0}^2/\Delta p_{st}$
Reference force	:	F_B	=	$\Delta p_{st} r m t$

Cross force

$$Q_i^* = \int_0^{2\pi} p_i^*(\varphi)\sin\varphi d\varphi$$

$$Q_{ges}^* = \sum_{i=1}^{m} Q_i^*$$

$$\overline{Q^*} = Q_{ges}^*/m$$

Dimensionless spring coefficient :

$$\overline{K_Q^*}(E_0^*) = d\overline{Q^*}/d\tfrac{e}{\Delta r}$$

Dimensioned spring coefficient :

$$K_Q = \overline{K_Q^*}\,\tfrac{F_B}{\Delta r}$$

Resulting labyrinth load :

$$Q = \overline{K_Q^*}\,\epsilon\,F_B$$

Restoring force

$$R_i^* = \int_0^{2\pi} p_i^*(\varphi)\cos\varphi d\varphi$$

$$R_{ges}^* = \sum_{i=1}^{m} R_i^*$$

$$\overline{R^*} = R_{ges}^*/m$$

(labyrinth mean value)

$$\overline{K_R^*}(E_0^*) = d\overline{R^*}/d\epsilon$$

$$K_Q = \overline{K_Q^*}\,\tfrac{F_B}{\Delta r}$$

$$R = \overline{K_R^*}\,\epsilon\,F_B$$

Figure 17: Definitions of test data analysis

M-Staggered-Labyrinth

Nr.	Typ	
1	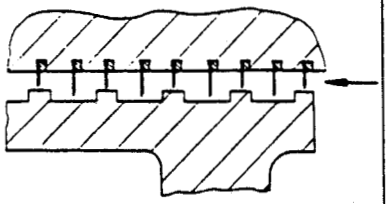	Number of cavities m=8 Inlet region: tooth on inflow
2	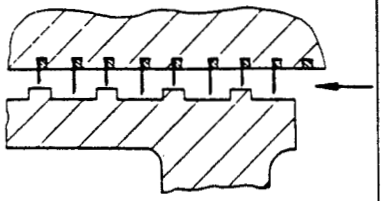	Number of cavities m=7 Inlet region: groove on inflow
3	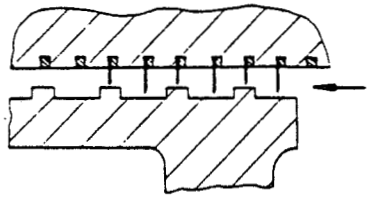	m=5
4	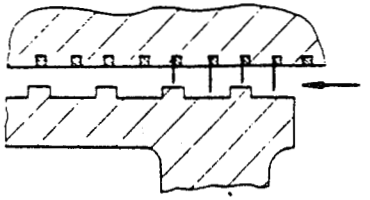	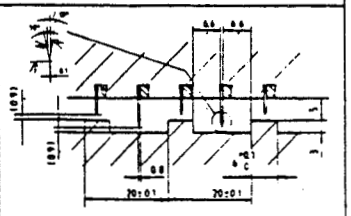 Φ D_s = 315 mm Δ r_N = 0,91mm Φ D_{RK} = 299 mm Δ r_K = 0,91mm Φ D_{RN} = 305 mm m=3

A-Full-Labyrinth

Nr.	Typ	
1	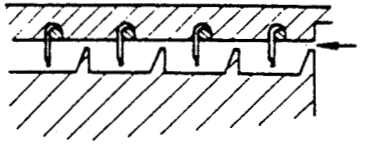	Number of cavities m=7 Inlet region: tooth on inflow
2	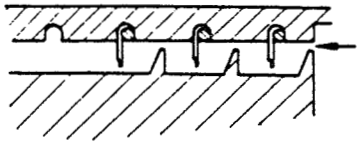	Number of cavities m=5 Inlet region: tooth on inflow
3	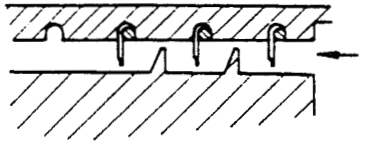	Number of cavities m=4 Inlet region: groove on inflow
4	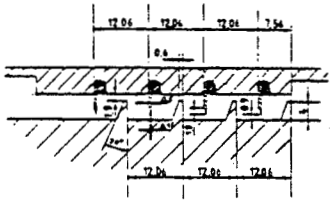	Φ D_s = 311,77 mm Φ D_{h2} = 307,9 mm Φ D_{h1} = 301,8 mm Φ D_R = 299,88 mm Δ r_N = 1,9 mm Δ r_K = 0,98 mm

Figure 18: M-staggered and A-full-labyrinth

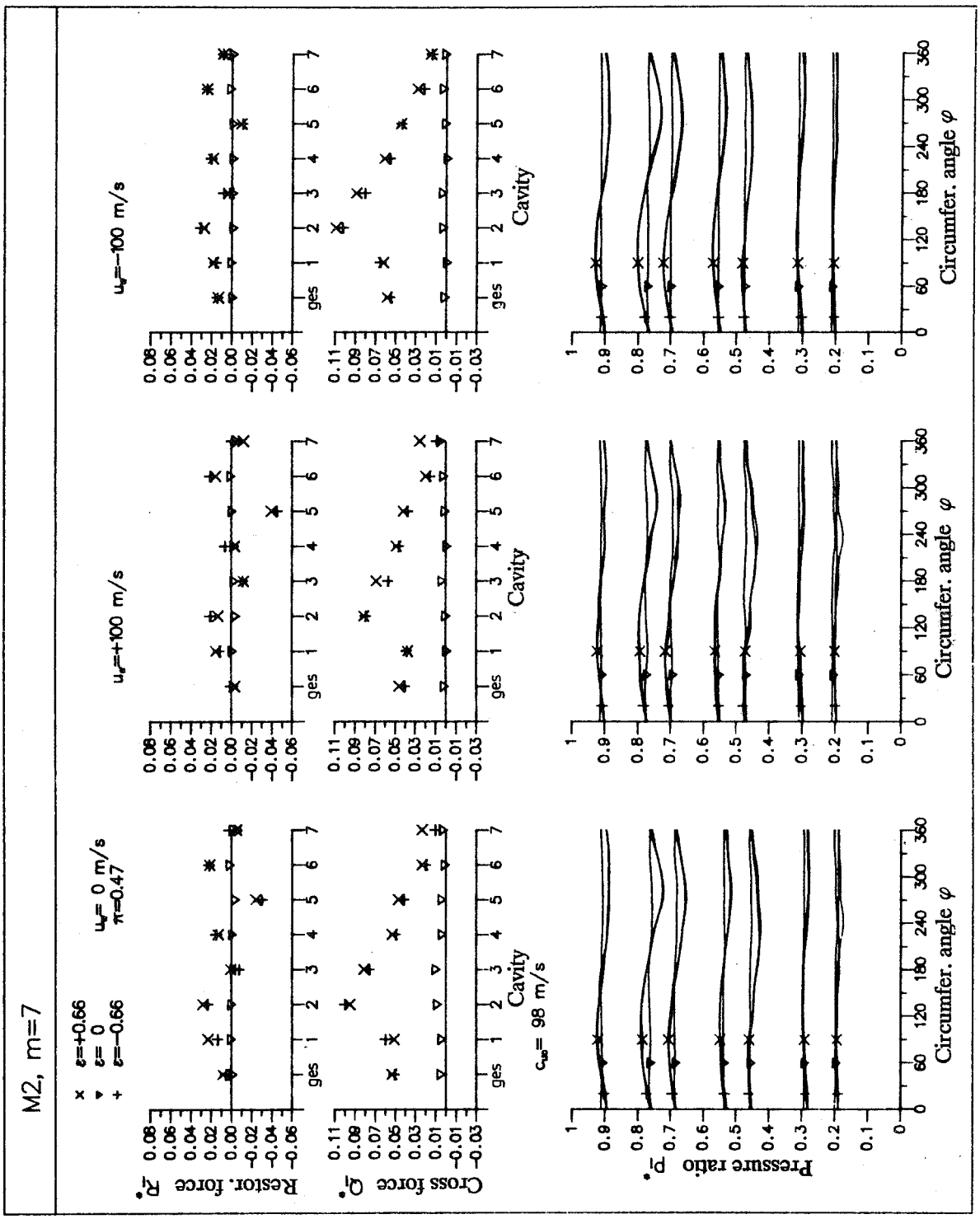

Figure 19: Characteristic of $p_i^*(\varphi)$, Q_i^*, R_i^* of M2

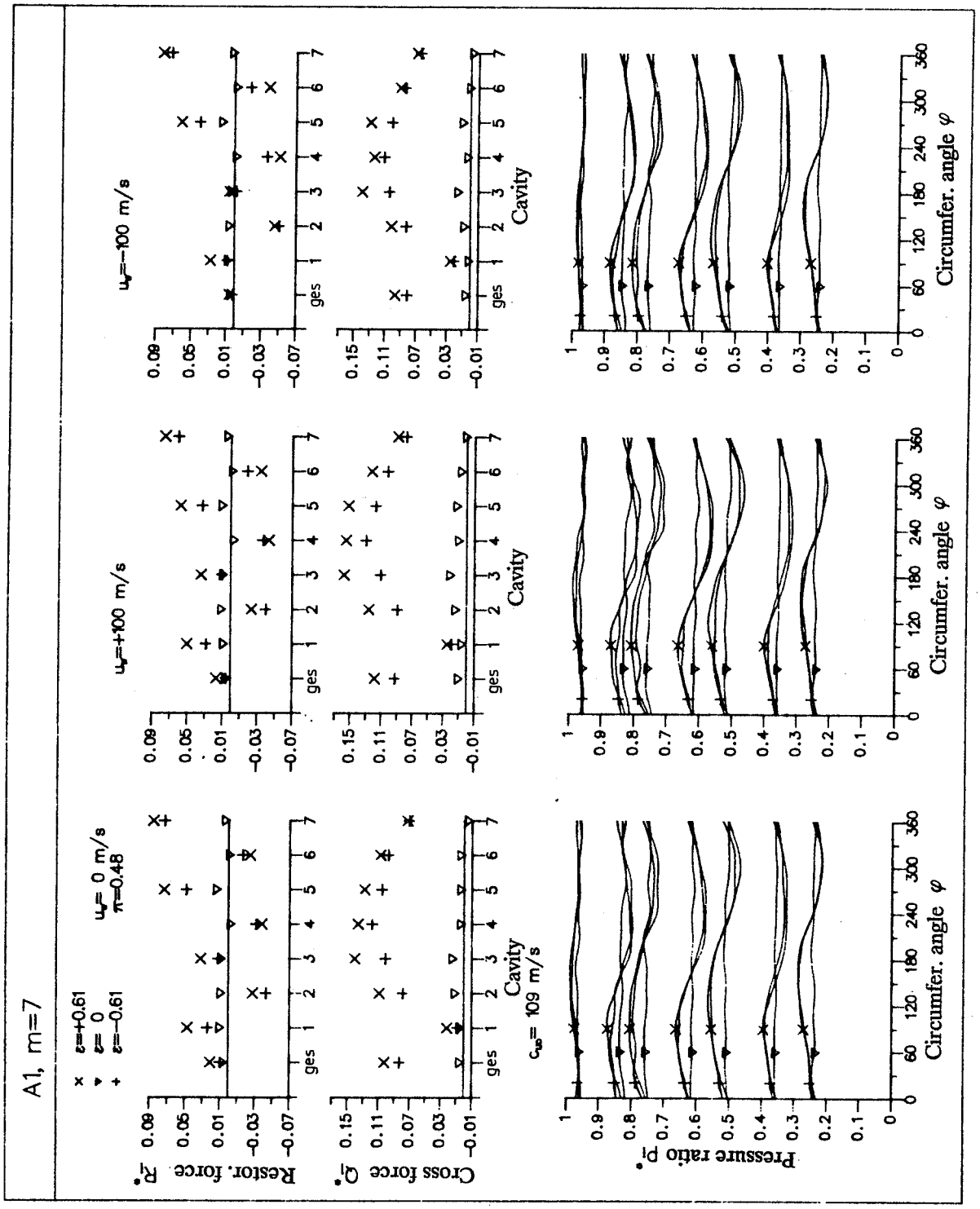

Figure 20: Characteristic of $p_i^*(\varphi)$, Q_i^*, R_i^* of A1

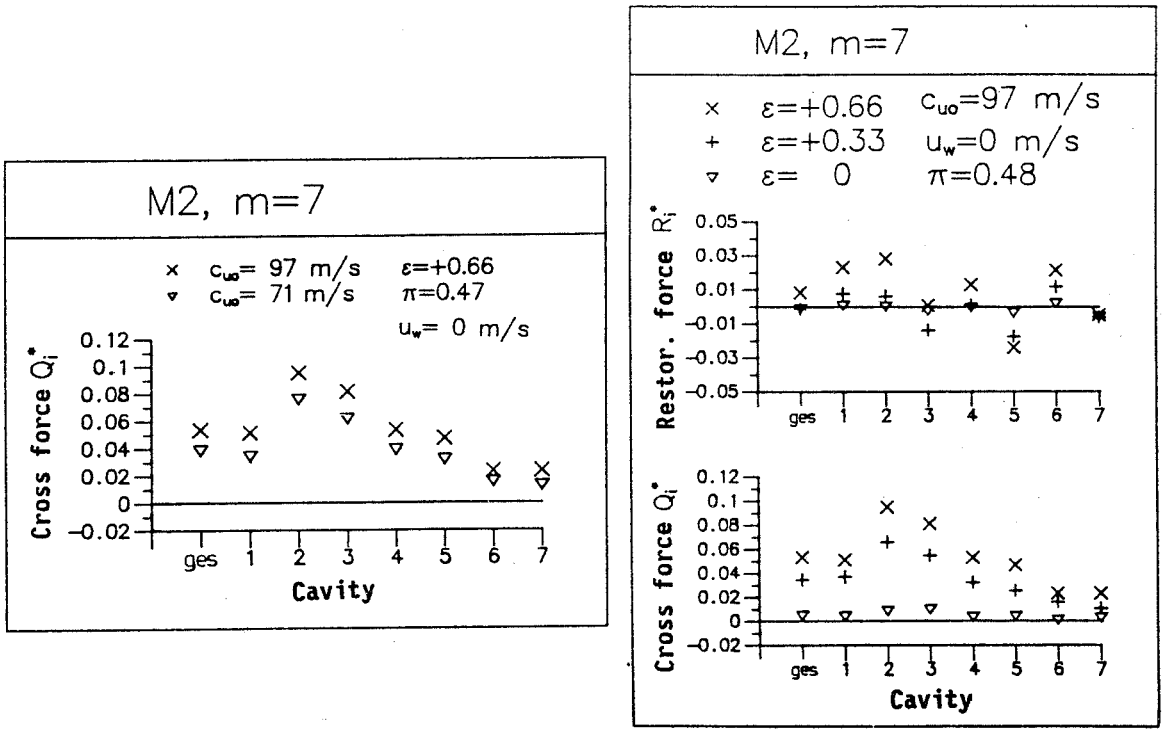

Figure 21: Q_i^* versus c_{u0}, ϵ of M2

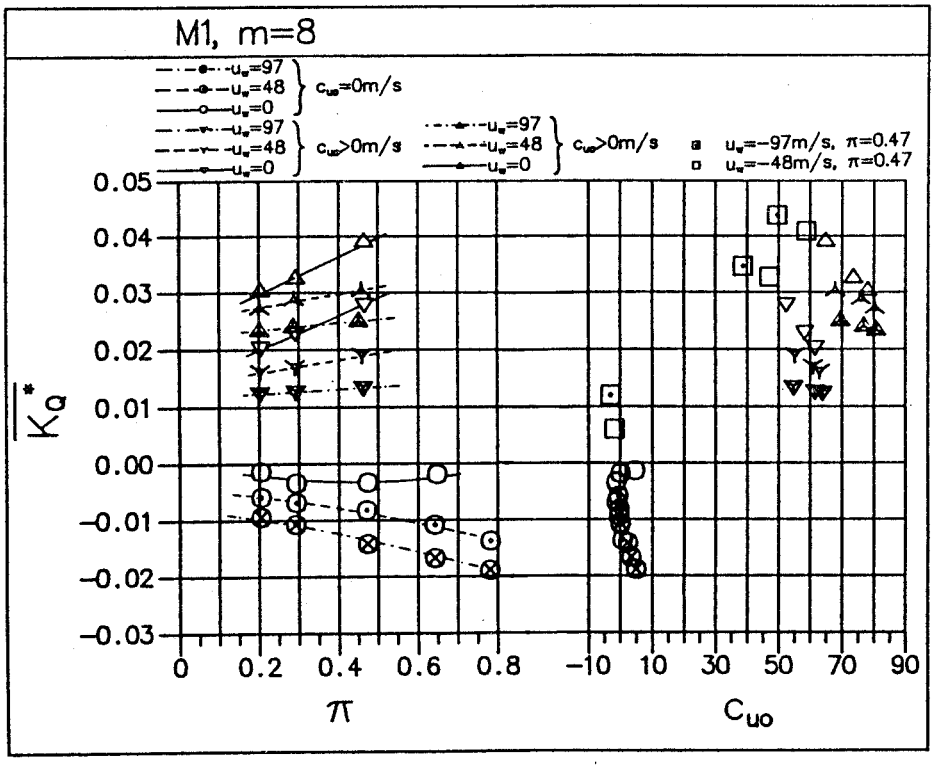

Figure 22: Characteristic field $\overline{K_Q^*}$ of M1

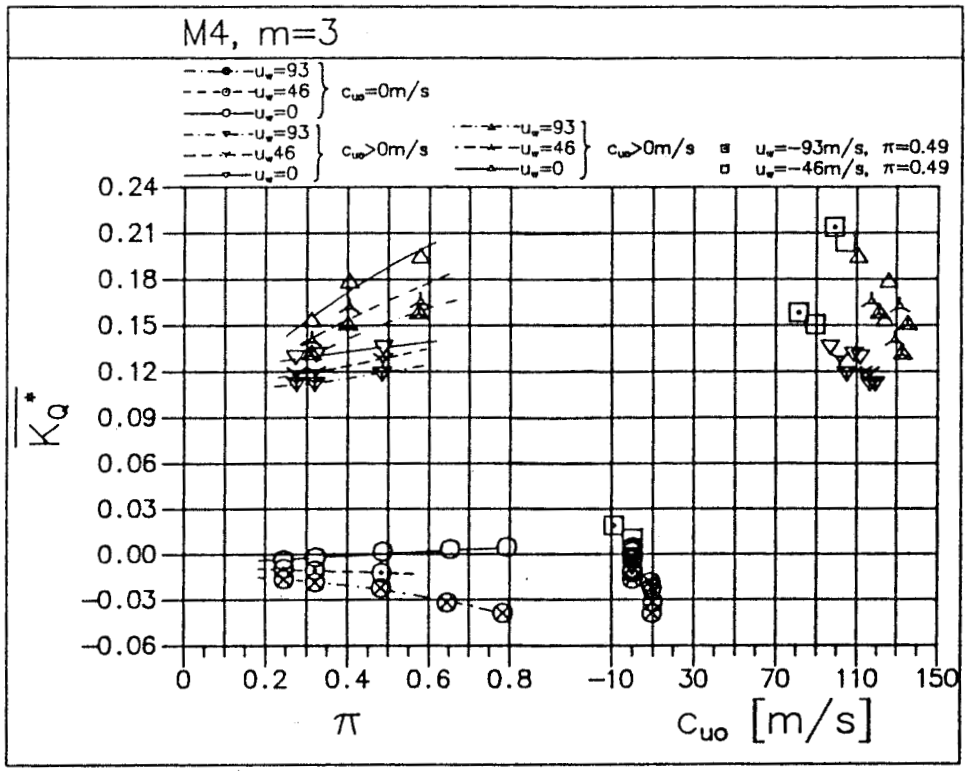

Figure 23: Characteristic field $\overline{K_Q^*}$ of M4

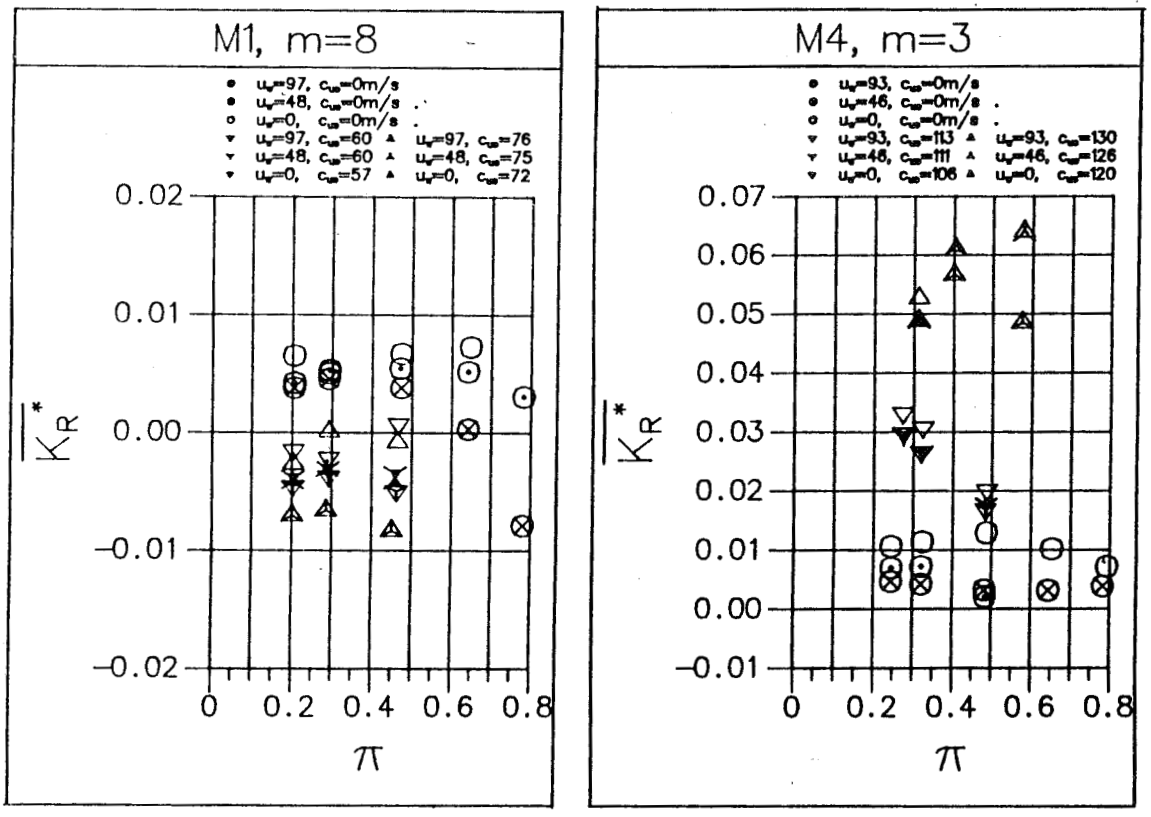

Figure 24: Characteristic field $\overline{K_R^*}$ of M1 and M4

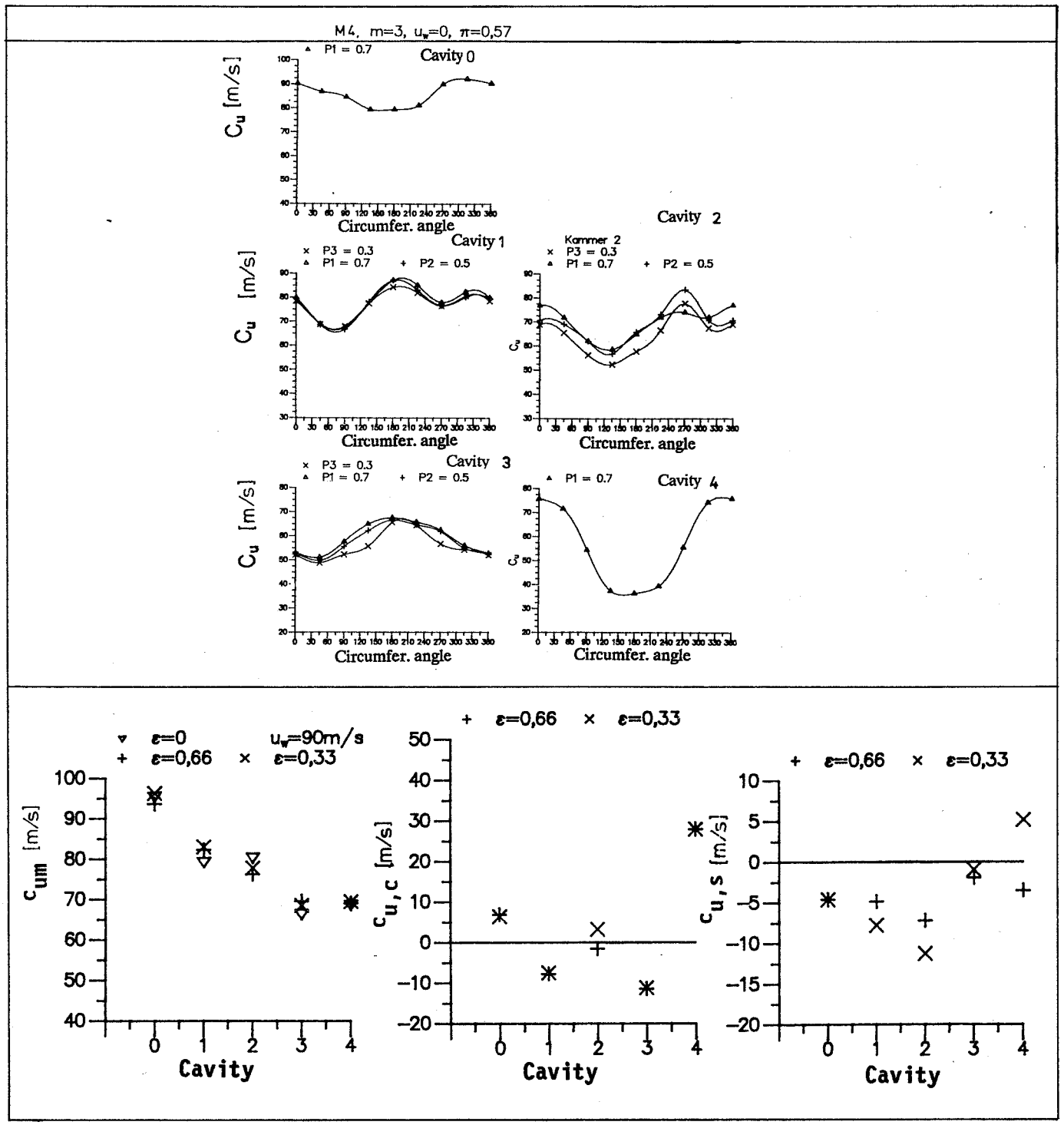

Figure 25: Circumferential velocity c_u versus cavity i and peripheral angle φ of M4